Non-lift-off Block Copolymer Lithography of 25 nm Magnetic Nanodot Arrays

A. Baruth,[†] Marc D. Rodwogin,[‡] A. Shankar,[†] M.J. Erickson,[§] Marc A. Hillmyer,*[,‡] and C. Leighton*[,†]

[†]Department of Chemical Engineering and Materials Science, [‡]Department of Chemistry, and [§]Department of Physics, University of Minnesota, Minneapolis, Minnesota 55455, United States

Ⓢ *Supporting Information*

ABSTRACT: Although nanolithographic techniques based on self-assembled block copolymer templates offer tremendous potential for fabrication of large-area nanostructure arrays, significant difficulties arise with both the lift-off and etch processes typically used for pattern transfer. These become progressively more important in the limit of extreme feature sizes. The few techniques that have been developed to avoid these issues are quite complex. Here, we demonstrate successful execution of a nanolithographic process based on solvent annealed, cylinder-forming, easily degradable, polystyrene-*b*-

polylactide block copolymer films that completely avoids lift-off in addition to the most challenging aspects of etching. We report a "Damascene-type" process that overfills the polystyrene template with magnetic metal, employs ion beam milling to planarize the metal surface down to the underlying polystyrene template, then exploits the large etch rate contrast between polystyrene and typical metals to generate pattern reversal of the original template into the magnetic metal. The process is demonstrated via formation of a large-area array of 25 nm diameter ferromagnetic $Ni_{80}Fe_{20}$ nanodots with hexagonally close-packed order. Extensive microscopy, magnetometry, and electrical measurements provide detailed characterization of the pattern formation. We argue that the approach is generalizable to a wide variety of materials, is scalable to smaller feature sizes, and critically, minimizes etch damage, thus preserving the essential functionality of the patterned material.

KEYWORDS: block copolymer, lithography, magnetic, nanodot array, PLA, NiFe
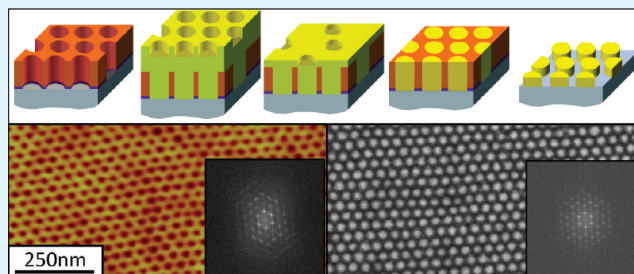
INTRODUCTION

Block copolymer (BCP) nanolithography has emerged as a powerful technique for the patterning of large-area nanostructure arrays in a wide range of functional materials. The self-assembled pattern in the polymer template can be transferred to the material of interest by a variety of schemes,[1] providing compatibility with many materials classes. Techniques designed to promote ordering of BCP templates (including spherical, cylindrical, and lamellar geometries) have progressed rapidly, driven by applications requiring long-range lateral ordering and high placement precision. Large-area magnetic nanodot arrays provide an illustrative example. From the technological viewpoint they are appealing for ultrahigh density bit-patterned magnetic recording media,[2] whereas from the fundamental viewpoint they enable basic studies of phase behavior and interactions in large statistical ensembles. In either case, the control of lateral ordering, placement precision, retention of robust ferromagnetism, and variations in dot-to-dot properties such as magnetic anisotropy are critical.

A variety of approaches have been used to promote such ordering of BCP templates. In terms of increasing long-range lateral ordering and correlation lengths, thermal annealing,[3,4] electric field alignment,[5,6] and incorporation of low-surface-energy midblocks[7] have proven constructive. For improvement of placement precision (i.e., registration), the use of prepatterned substrates
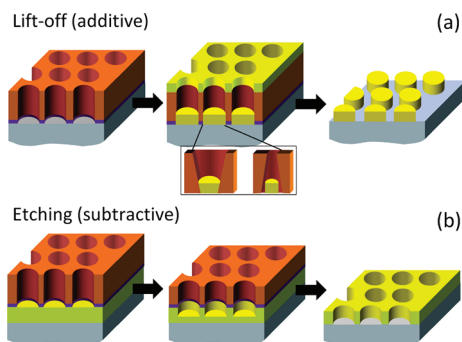
(chemical or topographical)[8−10] has been demonstrated effective. However, a dominant technique that has emerged (often in conjunction with another of the above-mentioned methods, primarily prepatterning) is solvent annealing.[4,11−16] This technique has the ability to dramatically reduce defect density, while improving both the perpendicular and lateral ordering more quickly and completely than previous methods. Of the self-assembled microstructures accessible in BCPs, cylinder-forming structures are particularly attractive for lithographic patterning, now that various methods have been developed to tailor the cylinder alignment with respect to the substrate surface.[1−11,13−16] It was recently shown for example[14] that long-range ordered (several micrometers), hexagonally close-packed, perpendicularly aligned cylinders could be achieved in polystyrene-*b*-polylactide (PS-PLA) thin films by solvent annealing in a neutral solvent vapor such as tetrahydrofuran (THF). In this process the solvent is thought to cause swelling of the polymer, in addition to mediation of the surface energies of the blocks. This lowers the glass transition temperature (T_g), increases mobility for mass transport, and may induce transient disorder. In the case of a neutral solvent, the surface energy for both blocks then becomes comparable,

Scheme 1. Schematic of (a) Lift-off (additive) and (b) Etching (subtractive) Lithographic Process; Inset to (a) Shows the Extremes of Side-Wall Profile; Left, Overcut; Right, Undercut

Scheme 2. Schematic Representation of the Fabrication of Nanoporous PS Templates: (a) Spin-Coating of PS-*b*-PLA in Chlorobenzene on HMDS-Treated, Natively Oxidized Si; (b) As-Spun Mixed Morphology; (c) Preparation of Perpendicularly Aligned PLA Cylinders with Hexagonal Short-Range Order Using THF Solvent Annealing; (d) Aligned Cylinders; (e) Degradation of PLA Minority Domains (cylinders) with a 0.05M NaOH Solution ($H_2O:CH_3OH$ = 6:4 by volume) and Subsequent Removal of Polymer Wetting Layer and HMDS by a 10 s O_2 reactive ion etch; (f) Final Template
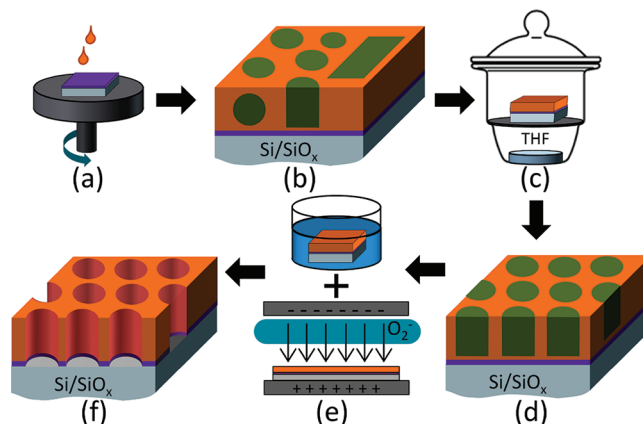

producing an ordering front at the polymer/vapor interface that favors perpendicular alignment of the cylinders, facilitates annealing of defects, and leads to strong lateral ordering that propagates through the bulk of the film as the solvent evaporates.[15−17] Although improvements to the polymer templates continue rapidly,[1] the demonstration of pattern transfer, with high fidelity and versatility, into disparate materials has been less explored.[7,18,19]

Generally, lithographic patterning schemes tend to fall into the broad categories of lift-off-based (i.e., additive)[3,20−22] or etching-based (i.e., subtractive)[7,23−27] approaches, as illustrated in Scheme 1. Both techniques have their advantages, although both also present certain drawbacks, particularly in the extreme feature size limit.[28,29] For example, lift-off is relatively simple and typically requires few steps, but places constraints on the possible deposition techniques (e.g., no high temperature growth). In addition, reproducibility and uniformity become very problematic when the pitch size of the template drops below 40−50 nm[3,20−22] due to difficulties in obtaining clean lift-off. This places high demands on difficult-to-control parameters such as the polymer template side-wall profile (see Scheme 1(a)). Conversely, etching processes are compatible with any deposition technique or prepatterning scheme, but the two dominant methods of etching also present significant difficulties. In wet etching (generally isotropic) it is difficult to control undercut, which leads to fast and uncontrolled destruction of the underlying film. In dry etching (generally anisotropic), milling or etching damage at the feature edges,[23−31] and redeposition effects,[32] pose well-documented problems that lead to suppression, or even complete destruction, of ferromagnetism. For example, in ref 30, they demonstrate, via high precision neutron reflectometry, the existence of a 75 nm wide 'dead' region surrounding a 200×400 nm^2 magnetic ellipse (i.e., feature sizes an order of magnitude larger than the presently studied structures) prepared by reactive ion etching. In addition to suppression of ferromagnetism due to damage, note that to form magnetic dots requires a second pattern reversal step, leading to further complications.

Recently, a pattern reversal process using a sphere-forming BCP was shown to produce ordered arrays of 17 nm Ni dots (which retain their ferromagnetism), improving upon existing schemes by avoiding a lift-off step and minimizing damage from physical milling.[33] However, this procedure required at least seven individual process steps, relied on two distinct pattern reversal processes, and the final magnetization was not quantified to determine retention of the magnetism. A single pattern reversal

mechanism has recently been demonstrated for the patterning of 14 nm wide metallic wires by a "Damascene" type process,[34] relying on six individual process steps.[35] However, a significant deviation from 'bulk-like' properties was reported in this case, specifically the resistivity increased considerably in comparison to bulk. Thus, although significant progress has been made, there remains much room for exploration, and successful demonstration, in the development of simple and reliable BCP pattern transfer schemes that avoid the common lift-off and etching/milling issues. This will only become more important as feature sizes are reduced.

In the current manuscript, we present a simple lithographic patterning scheme, based on solvent-annealed cylinder-forming BCPs, that is additive, yet avoids lift-off. The process is relatively simple, exploits facile aqueous degradation of the minority BCP component, and avoids some of the most problematic aspects to pattern transfer via etching, including etch damage, which is demonstrated by a retention of ferromagnetism that exceeds other traditional methods.[24,25] The process could be described as a "Damascene"-style overfill/planarize/etch-back scheme, exploiting the large physical etch rate contrast between the polymer template and typical ferromagnetic metals. This Damascene process ensures that the region of the metal film eventually forming the nanodot is well-protected from etching damage for a major fraction of the ion milling time, as the metallic overlayer acts as a protective overcoat. Successful lithographic patterning is demonstrated using the alloy $Ni_{80}Fe_{20}$ (NiFe) as a test case, further enabling magnetic and electronic transport characterization of the pattern transfer process, techniques that have proven useful in the past.[7] These techniques demonstrate a final array of NiFe nanodots that displays robust ferromagnetism, even at these size scales.

■ METHODS

Synthesis. A 75 mL pressure vessel equipped with a magnetic stir bar was charged with 2 g (5.0×10^{-5} mol) hydroxyl terminated
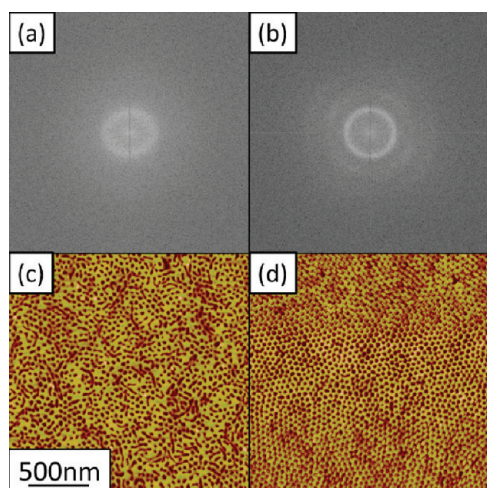
Figure 1. $2 \times 2 \, \mu m^2$ AFM images of the (c) as-spun and (d) solvent-annealed polystyrene template. (a, b) Associated fast-Fourier transforms shown above their respective AFM image.

polystyrene (M_n = 42.5 kDa) previously synthesized via living anionic polymerization. In a drybox, 14 mL of toluene and 5 μL of a 1 M AlEt$_3$ solution in heptane (5.0×10^{-6} mol AlEt$_3$) was added and the reaction mixture was allowed to stir 16 h. After stirring, 1.00 g (6.94×10^{-3} mol) D,L-lactide was added and the reaction was stirred for 24 h at 90 °C. The reaction was terminated with 2 mL of 1 M HCl$_{aq}$ and precipitated in methanol. The final polystyrene-*b*-polylactide had a total M_n = 63.7 kDa, with a PLA phase fraction of 0.29 (by volume) yielding a cylindrical morphology with a polydispersity index of 1.05. From small-angle X-ray scattering, the principle domain spacing, L_0, was 37 nm, leading to a minority cylinder diameter of 23 nm with a center-to-center distance of 43 nm.

Template Preparation. Solutions of 1.5% (w/v) PS-*b*-PLA in chlorobenzene were spin-coated onto hexamethyldisilazane (HMDS)-treated, natively oxidized silicon wafers. HMDS treatment of the Si wafers was carried out by ultrasonically cleaning substrates in organic solvents (acetone followed by methanol), treating them in a 1:5 (v/v) HMDS:toluene solution for 16 h, then rinsing in toluene and blowing dry with N$_2$ gas. The film was spin coated at 2000 rpm resulting in an incommensurate thickness of ~1.5L_0, an important parameter for perpendicular cylinder alignment (a commensurate thickness drives a trend toward in-plane cylinders)[13] that is dependent on both total molecular weight and volume fraction of PLA. Immediately following spin coating, two methods of solvent vapor treatment with tetrahydro-furan (THF) were carried out. In method A, a closed desiccator containing a 10 mL solvent reservoir was used, referred to as 'ambient'. Dependent on ambient conditions, solvent anneal times were optimized at 60−90 min (although long-range order was not observed). A similar anneal process was carried out successfully (i.e., perpendicular cylinder alignment with long-range lateral ordering) in ref 14 using the same block copolymer system; however, after hundreds of trials we were unable to reliably reproduce similar long-range lateral ordering with our material (a representative sampling is given in Figure S1 in the Supporting Information). We found that very high degrees of perpendicular cylinder alignment with short-range lateral ordering occurred for only ~10% of the attempts, all taking place under low humidity and more precisely controlled temperature conditions (i.e., in the winter months).This led us to explore the climate-controlled approach B, which led to a >50% success rate of achieving perpendicular alignment of cylinders with long-range lateral ordering (a representative sampling is given in Figure S2 in the Supporting Information). In method B, a sealed chamber (made completely of metal parts, i.e., no organic materials) was used to maintain

control of the solvent annealing climate (i.e., humidity, solvent vapor absolute and partial pressures, and anneal quench times), see Figure 6. The solvent annealing chamber (SAC) is tapped into a boil-off, dry N$_2$ line, which is split into two flow-controlled inlets. Inlet 1 is used to purge the sample space both before annealing and during the quench; this ensures a low-humidity environment during annealing and quick expulsion of the THF vapor during the quench. Inlet 2 is passed through a sealed solvent bubbler that carries solvent in the vapor phase into the sample space at a measured flow-rate. All flow into the sample space exits through a controlled-flow outlet to obtain sample space pressure control. Typical anneal times were 10 min, with a N$_2$ quench occurring in less than 1 s. The PLA minority domains were degraded with a 45 min soak in a 0.05 M NaOH solution (H$_2$O:CH$_3$OH = 6:4 by volume), followed by a 10 s O$_2$ reactive ion etch (60 W for 10 s in 30 mTorr) to remove both a polystyrene wetting layer[3] at the polymer/HMDS interface and the HMDS itself. The template fabrication process is detailed in Scheme 2. The final PS template for the ambient anneal case is representative of our best results under these conditions, showing perpendicular alignment of hexagonally close packed lateral local order cylinders. The thickness of this template is 48 nm, with a cylindrical pore size of 25.0 ± 2.8 nm and a center-to-center distance of 44.0 ± 3.8 nm (Figures 1 and 3). Improvements to the PS template were later made with the use of the SAC, where, as above, we present data representative of our best results. The same thickness was produced, and a pore size of 23.1 ± 2.5 nm with a center-to-center distance of 40.7 ± 1.7 nm was measured (Figure 6). NiFe deposition was done by molecular beam deposition from an alloy source at normal incidence with a source-to-substrate distance of 72 cm and a growth pressure of roughly 1×10^{-10} Torr. Nanostructure patterning was done via Ar ion beam milling (80 mA, 100 V, 8×10^{-5} Torr of Ar) at normal incidence, further described in the Results and Discussion.

Characterization. Scanning electron microscopy was performed on a Hitachi S-900 SEM with an accelerating voltage of 3.0 kV and atomic force microscopy was performed on a Digital Instruments Nanoscope III Multimode in tapping mode. Layer thickness was determined with grazing incidence X-ray reflectivity on a Panalytical X'Pert Pro with a CuKα source. Magnetic characterization was carried out on a Lakeshore vibrating sample magnetometer at room temperature under ambient conditions. Electrical characterization was done in a current source/voltage sensing 4-terminal van der Pauw geometry, where low resistance measurements (<100 Ω, t < 20 min in Figure 4) were done using an A.C. excitation current of 3×10^{-4} A and a D.C. excitation of 1×10^{-8} to 1×10^{-5} A was used for high resistance measurements (>100 Ω, $t \geq 20$ min in Figure 5).

RESULTS AND DISCUSSION

The template formation part of the process is illustrated in Scheme 2. The BCP templates (cylinder-forming PS-PLA; see Methods section for more details) were spun-cast from a 1.5% (w/v) chlorobenzene solution at 2000 rpm, resulting in 48 nm thick (~1.5L_0) mixed-orientation films (Figure 1a,c). Initial approaches based on solvent annealing in THF vapor for 60−90 min under ambient conditions (i.e., no control over humidity) led to perpendicularly aligned PLA cylinders with hexagonally close-packed lateral local order and significant improvement in the dispersion in pore size over as-spun films, as demonstrated by fast Fourier transforms of Atomic Force Microscopy (AFM) images (Figure 1b,d and discussion in the Methods section). Further improvements to the solvent annealing process will be discussed below. The PLA minority domains are then degraded in a weak basic solution, and a polystyrene wetting layer[3] at the polymer/substrate interface, as well as the HMDS adhesion layer, was removed using a 10 s oxygen reactive ion etch. The template
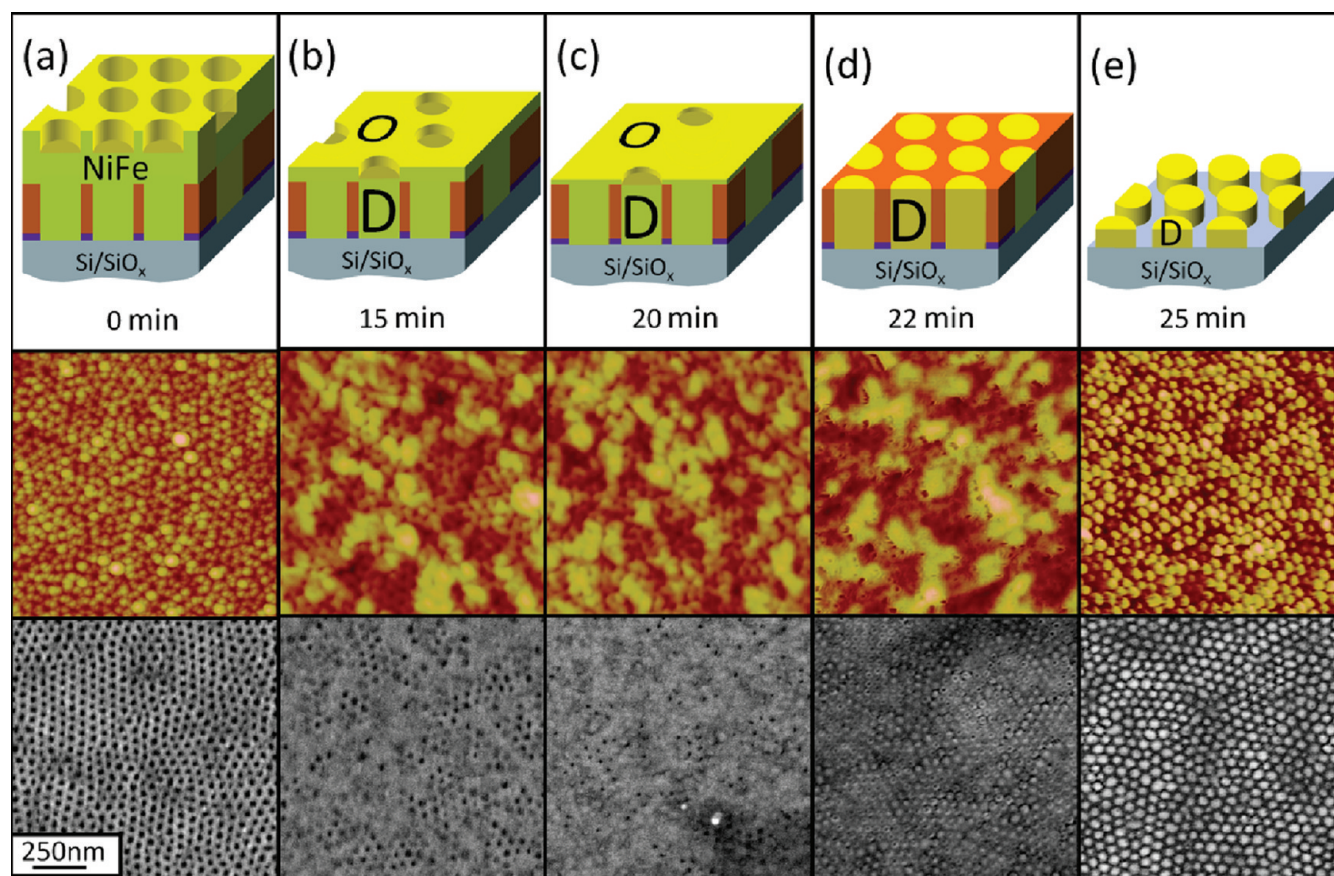
Figure 2. Schematics (top panel), tapping mode AFM images (center panel), and SEM images (bottom panel), of NiFe deposited onto a PS template at critical times during the Ar ion milling process, as illustrated in the top row: (a) 0 min (after NiFe deposition); (b) 15 min (NiFe film is planarized, with the overlayer "O" and dimple "D" regions indicated); (c) 20 min (further planarization of NiFe, overlayer persists); (d) 22 min (milling into the PS template); (e) 25 min (final NiFe dot array). All images are $1 \times 1\ \mu m^2$. The z-scale of the AFM images is 10 nm for a–d and 25 nm for e.

thus formed is then used in an additive process which avoids a final lift-off step. The pores are first overfilled (to a 43 nm excess) by NiFe evaporation. The NiFe overlayer is then planarized by normal incidence Ar ion beam milling, and etched back to reveal the underlying polymer template. The large etch rate difference between polymer and metal then enables formation of a metal dot array. In Figure 2, the metal patterning process is shown at five critical steps: (a) after 70 nm NiFe deposition onto the PS template, (b) after 15 min of Ar ion beam milling (leading to an approximately planarized NiFe surface), (c) after 20 min of Ar ion beam milling (near complete removal of dimpled regions, but some persistence of the overlayer, (d) after 22 min of Ar ion beam milling (the initial stages of removal of the PS template), and (e) after 25 min of milling (the final NiFe dot array).

In Figure 2, the top panel shows schematics while the middle and bottom panels show $1 \times 1\ \mu m^2$ AFM and SEM (scanning electron microscopy) images, respectively. From Figure 1d, we see that the cylindrical pores orient perpendicular to the surface and have a diameter of 25.0 ± 2.8 nm (see Figure 3, inset) and a center-to-center distance of 44.0 ± 3.8 nm, consistent with measurements on the bulk PS-PLA (see Methods section). As shown in Figure 2a, the UHV evaporation (see Methods section for details) of 70 nm of NiFe results in overfilling of the pores, the overlayer appearing to "contour" the underlying PS template. Note that the overlayer "dimples" have decreased diameter in comparison to the initial template pores (Figure 1d), as expected.

A naïve view would suggest that Ar ion beam milling at normal incidence would maintain this conformal pattern through the entire milling process, yielding no pattern transfer to the NiFe layer. However, because of effects such as resputtering occurring within the dimple features, planarization of the surface occurs (a well-documented phenomenon[36–38]). By 15 min of milling (Figure 2b) more than 80% of the dimples are no longer visible with the remainder being considerably shallower than in the original overlayer (Figure 2a), as indicated by the weaker contrast and smaller diameter in AFM and SEM images. This is further confirmed below by measurements of the surface roughness. The planarization of the NiFe surface continues through 20 min (Figure 2c, where more than 95% of the dimple features are obliterated), up to 22 min (Figure 2d), at which point the PS template is close to fully uncovered and a distinct change in surface morphology occurs. The SEM image (Figure 2d) clearly shows the removal of the PS matrix, revealing the formation of isolated dots (formerly dimpled regions) in conjunction with a network of NiFe interstices atop the PS. Importantly, from the accompanying AFM image it can be seen that at this stage the dimple features are almost gone, although some thickness variations in the remaining PS/NiFe layer are apparent. These thickness variations are likely the cause for the dispersion in diameters of the final NiFe dot array, as discussed below. In the final step (Figure 2e), the fact that the relative mill rates of the PS template (>10 nm/min) and the NiFe (~2 nm/min) differ by a
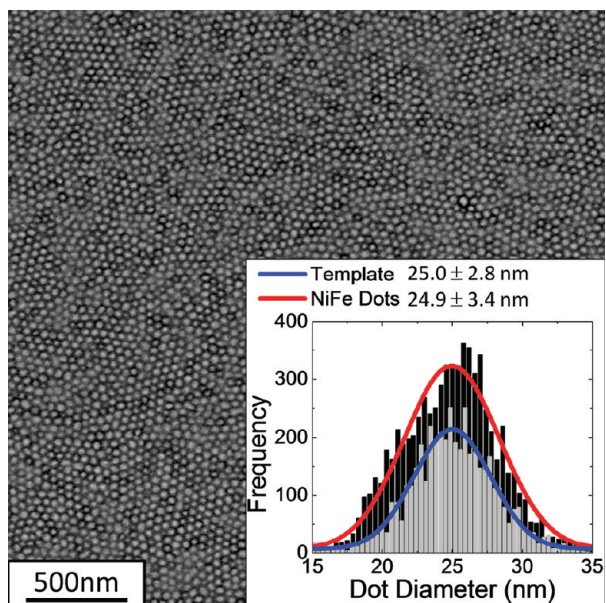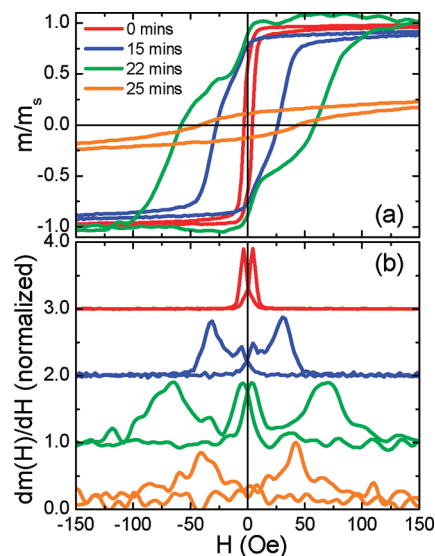
Figure 3. (a) Representative SEM image ($3 \times 3\ \mu m^2$) of the final NiFe dot array (corresponding to Figure 2e). The inset histogram gives the distribution of diameters of the initial PS template (for a $4 \times 4\ \mu m^2$ image) in gray and the final NiFe dot array (for a $6 \times 6\ \mu m^2$ image) in black. The solid lines are Gaussian fits for the template (NiFe dots) yielding an average diameter of 25.0 ± 2.8 nm (24.9 ± 3.4 nm).

Figure 4. (a) Normalized room-temperature magnetic moment, m/m_s, versus applied field, H, for representative mill times showing each of the four regimes discussed in the text. (b) Derivatives with respect to applied field normalized by the maxima, in a cascade plot. The two intermediate mill times (15 and 22 min) display two distinct switching fields (confirmed by $dm(H)/dH$ in b) corresponding to the NiFe overlayer (smaller coercivity) and dimple regions (larger coercivity).

factor of 5 is exploited. The PS template is thus quickly removed by the Ar ion beam milling (thus minimizing exposure of the NiFe dot features to the Ar ions), leaving a dot array formed from the more slowly milled NiFe. Note that until the final 3 min of milling, this technique ensures that the dot regions were well-protected from the Ar ions by the overlayer.[36,37]

A representative large-scale SEM image of the final NiFe dot morphology is presented in Figure 3 (multiple images across a 5 mm × 5 mm sample showed no qualitative differences). Consistent with the template shown in Figure 1d, the final NiFe dot array exhibits local hexagonal close-packed order. Image analysis[39] results in the histograms shown in the inset (0.5 nm bin size) for the template and dot array. The results reveal an average dot diameter of 24.9 nm with a standard deviation of 3.4 nm, which can be compared to the initial PS template with an average diameter of 25.0 nm and a standard deviation of 2.8 nm. The center-to-center distance of the dot array is 43.1 nm with a standard deviation of 3.6 nm, consistent with the original template, as expected. Note the slight skew toward smaller dot sizes when compared to the initial template, consistent with the small increase in standard deviation. This is due to the imperfect planarization of the NiFe layer discussed above (Figure 2c), and the minor thickness variation shown in Figure 2d, which led to over etching of some of the NiFe dot features. Further refinement of the planarization process (e.g., by off axis milling, sample rotation, thicker metal layer deposition, or the use of multiple etch/planarization layers) as well as improvement to the PS templates could potentially improve this. The latter is demonstrated below.

Although the surface characterization techniques (i.e., AFM and SEM) are strongly indicative of successful patterning, the use of a ferromagnetic metal allows additional characterization of the fidelity of the patterning process,[7] in addition to providing proof of the retention of ferromagnetism. For instance, the magnetic

moment (m, normalized to the saturation value m_S), as a function of applied field (H) provides a useful, nondestructive tool for characterization of the patterning process as it allows for separation of the magnetic signatures arising from the material within the dimpled regions from that of the remaining overlayer. A similar approach was used in ref 40. Figure 4a shows four representative $m(H)$ hysteresis loops, whereas Figure 4b displays the corresponding derivatives $dm(H)/dH$, each taken at different mill times. At $t = 0$ (i.e., immediately after NiFe deposition on the template), a single coercive field ($H_C = 4$ Oe) is observed, indicative of a single-step switching process, as expected. Note that H_C is slightly elevated in comparison to films grown on clean inorganic substrates, but is consistent with witness NiFe films grown on PS homopolymer (see Figure S3 in the Supporting Information). At intermediate mill times (i.e., $t = 15$ and 22 min), two distinct coercive fields (and thus switching events) are observed in $m(H)$ (Figure 4a), confirmed by peaks in $dm(H)/dH$ (Figure 4(b)). In all cases where two distinct H_C values are observed, the lower value was consistently around 4 Oe, indicating that it is associated with the NiFe in the regions on top of the PS template. Proof that this low H_C contribution is associated with an overlayer is provided by Figure S3 in the Supporting Information, which shows the results of a control experiment where a uniform (unpatterned) NiFe film on a PS underlayer is progressively etched. The initial NiFe thickness (43 nm) was chosen to match the overlayer thickness in the pattern transfer case, while the PS molecular weight ($M_n = 42.5$ kg/mol) and spinning conditions were also kept similar. As can be seen from the figure, H_C is low (below 2 Oe in this case) at all mill times, demonstrating that the low H_C component can be unambiguously associated with the uniform overlayer. Hence, as illustrated in the schematic in Figure 2c, the low H_C regions are designated as the "O" (overlayer) regions. The larger, mill-time dependent value of H_C corresponds to the NiFe in the "D"
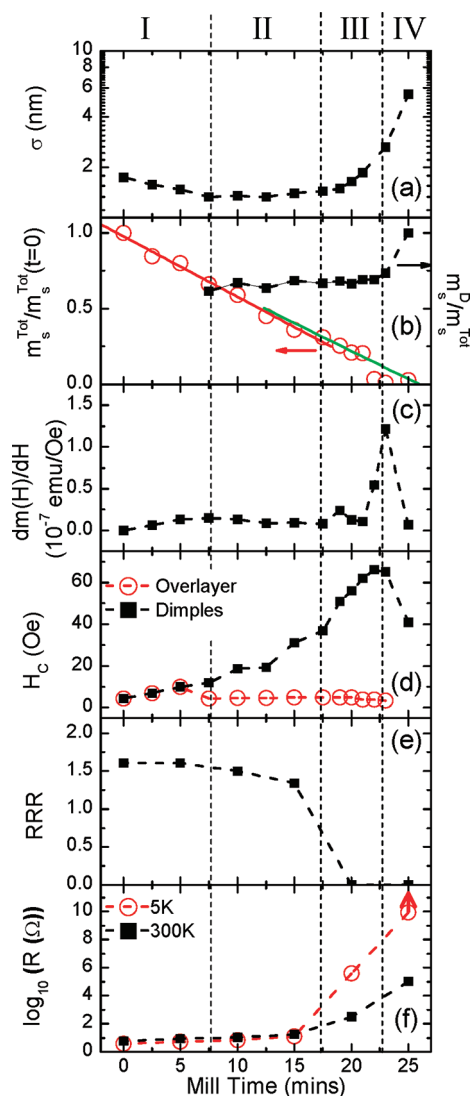
Figure 5. Ar ion beam milling time dependence of (a) the rms roughness (σ) from $2 \times 2\,\mu m^2$ AFM images; (b) the 300 K saturation moment for the full structure, normalized by the $t = 0$ value (red open circles), and the fraction of the moment attributed to the dimpled regions (black solid squares); (c) the high field slope ($dm(H)/dH$) of the raw moment versus applied field—contribution from substrate is subtracted; (d) the coercivity of the NiFe overlayer (red open circles) and dimpled regions (black solid squares), (d) the residual resistivity ratio; and (e) $\log_{10}$ of the four-terminal resistance measured at 300 K (red open circles) and 5 K (black solid squares). The data are broken up into four regimes, as described in the text. Dashed lines are a guide to the eye. In (b), the solid red line is a linear fit to regimes I and II, whereas the solid green line is a linear fit to regime III.

(dimpled) regions (see Figure 2b−e). These are the regions that eventually form the final NiFe nanodots (Figure 2e). At $t = 25$ min, i.e. after the milling process is complete, the low H_C shoulder vanishes, as expected when the O regions have been completely removed, leaving only the final NiFe dot array. The distributions in dot diameter and thickness (which must lead to distributions in volume and magnetic anisotropy energy) result in a distribution of switching fields and remanent magnetization values, giving rise to the broad reversal behavior observed in $m(H)$. Below, we will show how further optimization of the PS

templates can significantly reduce this distribution. The existence of distinct switching fields at intermediate mill times allows us to uniquely separate the two magnetic contributions (from the O and D regions), and track their coercivities and individual magnetic moments as a function of mill time.

Figure 5 provides a complete characterization of the patterning process, via the Ar ion beam milling time (t) dependence of (a) the rms roughness (σ), calculated from $2 \times 2\,\mu m^2$ tapping mode AFM images, (b) the measured total magnetic moment (m_S^{Tot}), normalized to the value at $t = 0$ ($m_S^{Tot}\,(t = 0)$) (left axis), and the fraction of the magnetic moment due to the D regions (m_S^D) relative to m_S^{Tot} (right axis), (c) the high H (2 kOe) slope of the $m(H)$ loop, (d) the H_C of the O and D regions, (e) the residual resistivity ratio $[RRR = R(300\text{ K})/R(5\text{ K})]$, and (f) the resistance measured at 300 and 5 K using the 4-terminal van der Pauw method. These t-dependent properties reveal four distinct regimes, indicated by the vertical dotted lines in Figure 5.

In regime I ($0 < t < 7.5$ min), there is a slow decrease in σ with t (Figure 5a), confirming the planarization of the NiFe overlayer discussed above in connection with Figure 2. During this period, the hysteresis loops exhibit a single H_C (see Figure 5d), which increases only weakly with t, in addition to an m_S^{Tot} that decreases linearly with t (Figure 5b). This is all consistent with etching of a progressively planarized NiFe overlayer. Note that the high field slope of the hysteresis loop (Figure 5c) is close to zero in this regime, as expected for a conventional ferromagnet with low H_C. No large changes occur in either the R or RRR values, as expected.

The milling process continues into regime II ($7.5 \leq t < 17.5$ min), with little modification of the surface morphology, as evidenced by the relatively constant σ (Figure 5a). On the basis of the $m_s^{Tot}(t)$ (Figure 5b, left axis) in this regime, and regime I, a mean mill rate (averaged over both O and D regions) is estimated at 2.3 nm/min, consistent with the value obtained from milling a planar NiFe layer (2.1 nm/min, see Figure S3 in the Supporting Information). The entry into regime II also marks the first point at which the hysteresis loops clearly display two distinct H_C's. As discussed above (Figure 4) the smaller of these ($H_C \approx 4$ Oe) is attributed to the continuous NiFe overlayer atop the PS template (the O regions). The larger H_C results from the NiFe within the dimple features (the D regions); i.e., the regions that eventually form the NiFe nanodots. The fact that two distinct H_C values are observed indicates that, as early as $t = 7.5$ min, we observe two distinct magnetization reversals from the O and D regions. This becomes progressively more apparent with increasing t. As t increases the H_C of the D regions increases, as expected when the thickness of the overlayer approaches "pinch-off" of the O and D regions.

As shown on the right axis of Figure 5(b), m_S^D/m_S^{Tot} (i.e., the fraction of the magnetic signal arising from the D regions) increases only weakly with t in this regime (with a slope 0.0047 ± 0.0031 min^{-1}), reflecting the fact that the O and D regions are milled at comparable rates. This is substantiated by the relatively constant surface roughness across this regime (Figure 5a). To put these values in context, note that the area fraction of the nanopores in the original template (Figure 2d) is 0.46 (the increase over initial phase fraction due primarily to the O_2 RIE process), leading to a volume fraction of the D regions of 0.64 at $t = 7.5$ min, i.e., the entry into regime II. This is computed assuming that the D regions are pillars that span the entire metal film with the same area fraction as the voids in the template. Reassuringly, the experimental m_S^D/m_S^{Tot} values are close to this expected

value in regime II (Figure 5(b)). The high field slope of $m(H)$ in region II is again close to zero, as expected. Panels e and f in Figure 5 show that R exhibits an initial weak increase with t in regime II, accompanied by a slight decrease in RRR, simply attributed to a decrease in thickness of the NiFe overlayer, possibly in addition to some increase in defect density with ion milling. As discussed below, the electronic properties change dramatically on entry to regime III.

In regime III (17.5 min < t < 22.5 min), the O regions become progressively diminished and, eventually, the PS template becomes exposed over a significant majority of the film area for the first time (Figure 2d). It is important to note that even at the point where the O and D regions "pinch-off", the O regions still provide significant magnetic signal, as evidenced by panels b and d in Figure 5. This is expected in the ideally planarized case; however, lateral nonuniformities from the milling process will enhance this effect. When the PS becomes exposed over a large fraction of the surface the much faster mill rate of the PS (>10 nm/min) compared to the NiFe ($\sim$2.3 nm/min) results in a significant upturn in σ (a factor of 5 increase over the planarized film occurs in regime III), as the slowly milled NiFe protrudes from the PS surface (Figure 2d). In this regime m_S^{Tot} begins to deviate from the initial mill rate calculated in Regimes I and II, from 2.3 nm/min to 1.6 nm/min, as indicated by the green solid line in Figure 5b. m_S^D/m_S^{Tot} continues its monotonic increase with t (slope = 0.010 ± 0.003 min^{-1}). The H_C of the D regions increases as "pinch-off" is approached, while H_C remains nearly constant for the overlayer (consistent with a planar NiFe film; see Figure S3 in the Supporting Information). At least initially, any change in the high field slope of $m(H)$ remains negligible in this regime.

The electrical properties respond dramatically between t = 15 and 20 min, much more so than the magnetic ones. As shown in panels e and f in Figure 5, the NiFe film resistance reveals an abrupt increase at this time, the 5 K R value increasing by more than 4 orders of magnitude.[41] At this point the $R(T = 5 K)$ value actually exceeds $R(T = 300 K)$, and the RRR falls dramatically to values below 1, indicating strongly insulating transport behavior, in sharp contrast to the originally metallic behavior of the NiFe overlayer. These data thus indicate that the onset of insulating transport occurs prior to complete eradication of the overlayer judged from magnetometry data (see Figure 5b,d). This is fully expected because of the nonintegrative nature of the transport. The two-dimensional percolation threshold is reached well before the O regions are completely removed, meaning that insulating transport occurs prior to loss of magnetic signal from the O regions. At a later time, toward the end of regime III, around t = 21−22 min, m_S^{Tot} displays an abrupt, steplike decrease (Figure 5b), accompanied by the onset, for the first time, of a noticeable high field slope in the $m(H)$ loops (Figure 5c). This occurs when the isolated interstitial O regions (post "pinch-off") become reduced in volume to the point where they become thermally unstable, i.e., superparamagnetism occurs. This results in the high field slope in $m(H)$ in 300 K measurements.

The crossover region between regimes III and IV is revealed most strikingly in Figure 5b−d. In particular, the high field slope in $m(H)$ vanishes and m_S^D/m_S^{Tot} abruptly approaches 1. These observations indicate the formation of isolated NiFe nanodots that retain ferromagnetism, the magnetic signal (including any superparamagnetism) from the O regions being completely eradicated. Interestingly, at this point the coercivity (Figure 5d) drops, indicating a slight decrease in thermal stability when the
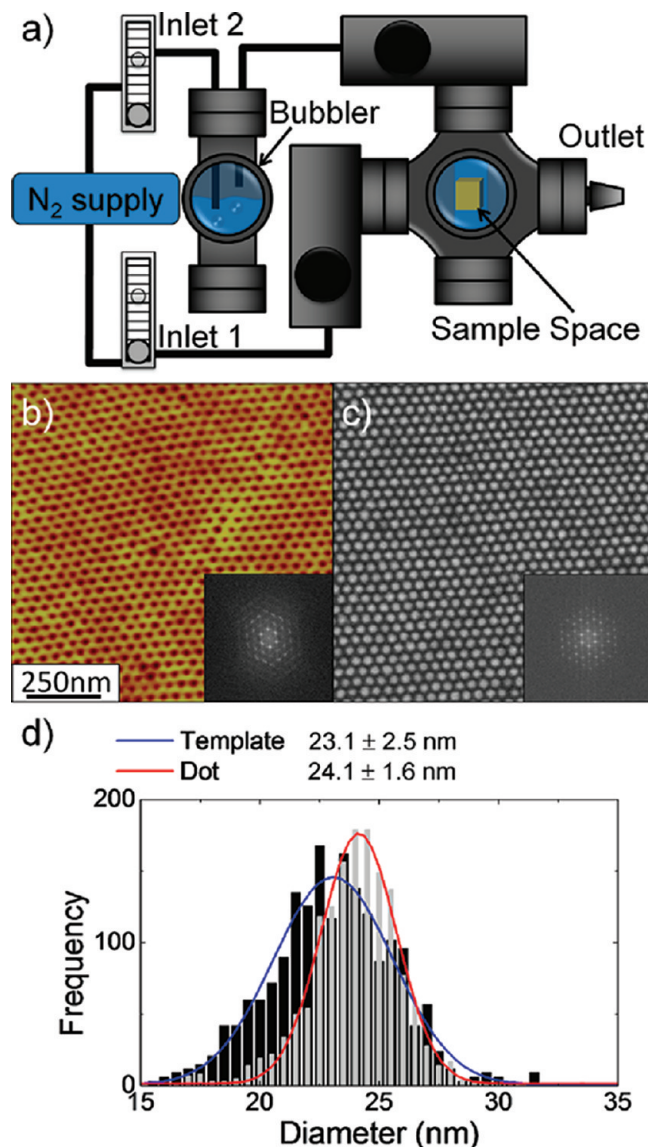
Figure 6. Formation of a NiFe nanodot array using climate-controlled solvent annealed, long-range ordered, hexagonally close packed poly-(styrene-b-lactide) templates. (a) Schematic representation of the solvent anneal chamber, with two flow-controlled inlets, (1) dry N$_2$ for purging the sample space and (2) dry N$_2$ solvent bubbler to carry saturated solvent vapor into the sample space, and one flow-controlled outlet.(b) $1 \times 1 \mu m^2$ AFM image of an optimized polystyrene template, where the inset is the fast Fourier transform. (c) SEM image of the NiFe nanodot array formed after a 20 min Ar mill from the optimized template in b, where the inset is the fast Fourier transform. (d) Histograms giving the distribution of diameters of the initial PS template (for a $2 \times 2 \mu m^2$ image) in black and the final NiFe dot array (for a $1.5 \times 1.5 \mu m^2$ image) in gray. The solid blue (red) line is a Gaussian fit for the template (NiFe dots) yielding an average diameter of 23.1 ± 2.5 nm (24.1 ± 1.6 nm).

overlayer is completely removed. Finally, the t = 25 min R value, measured at 5 K, is beyond the 10 GΩ measurement capabilities of our setup (for reference, this value is plotted in Figure 5f), giving a minimum value of R for the final nanodot array. This is a strong indicator of electronically isolated metallic nanodots over large lateral length scales.

When interpreting the magnetic behavior displayed by the final dot array (25 min milling, Figure 4a), it is important to
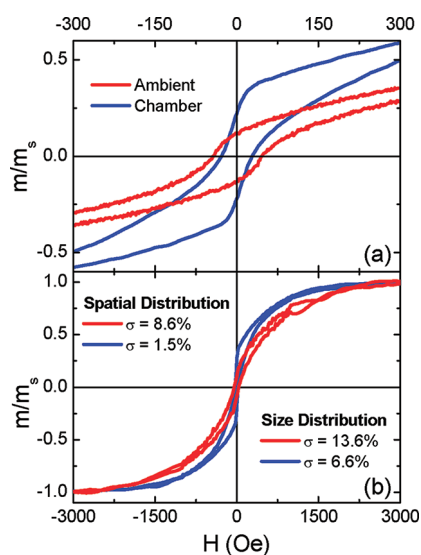
Figure 7. (a) Normalized magnetic moment, m/m_s, versus applied field, H, for two NiFe nanodot arrays on two applied field scales (300 Oe in panel a, 3000 Oe in panel b) at 300 K. The magnetic moment from nanodots derived from an ambient solvent annealed template are shown in red, whereas nanodots derived from the climate-controlled solvent annealing chamber-based template are shown in blue. The corresponding distribution in nanodot position and diameter are also given as an inset to b.

understand the approximate location on the phase diagram of ferromagnetic nanodots. Using an attempt frequency of 1×10^9 Hz, a measurement time of order 100 s, and a magnetocrystalline anisotropy constant of 3×10^3 erg/cm^3,[42] the Néel-Arrhenius model[43] predicts a transition to superparamagnetism at a thickness of 13 nm for the diameters studied here (25 nm). (Note that shape anisotropy, which is significant in this case because of the low magnetocrystalline anisotropy of NiFe, has been taken into account in a self-consistent manner[44]). Simple estimates of the single domain to multidomain crossover for a 25 nm diameter NiFe dot suggest a crossover thickness of ~20 nm.[45] These values should be compared to the thickness, or height, of the final dot array, which was determined to be approximately 17 nm by X-ray reflectivity. These dots are thus just above the critical volume for a transition from ferromagnetism to superparamagnetism, and just below the transition from a single domain to multi-domain crossover. It is thus expected that the relatively large distribution in dot diameter (13.6%) leads to significant variation in the phase behavior of individual dots. In particular, a substantial fraction of these dots are expected to be superparamagnetic on these time scales, leading to broad distributions in local magnetization and switching field, consistent with Figure 4. Although it is difficult to simply determine the saturation magnetization in this case, our best estimates lie at $M_s \approx 315$ emu/cm^3 (i.e., 40% of bulk), where the reduction is due, in part, to etch damage, but also a significant fraction of the material becoming superparamagnetic. To put this value in context, an upper bound of ~45% in magnetization retention was shown for Ar ion beam milling pattern transfer of 25 nm CoCrPt dots, this value dropping quickly with additional milling.[25] In addition, a comprehensive study of magnetization retention as a function of CoPt dot diameter (40−100 nm), again produced by Ar ion beam milling, suggests a saturation magnetization less than 25% of the bulk value at the lower end of feature sizes.[24] Clearly, our large size

distribution array, obtained from 'ambient' solvent annealing, is similar or better, in terms of magnetization retention, than the smaller size distribution examples reported in the literature (produced from materials with significantly larger magnetocrystalline anisotropy). Next, we demonstrate that the Damascene approach of pattern transfer is capable of even better magnetization retention for nanodot arrays obtained from the more ordered, climate-controlled solvent annealed templates.

Although the above data clearly demonstrate a simple means to achieve non-lift-off, high-fidelity pattern transfer and retention of ferromagnetism, the templates employed possess only short-range hexagonal order and exhibited broad distributions in size and magnetic response. In order to improve upon this, additional experiments were carried out under climate controlled conditions as opposed to ambient. As shown in Figure 6a, a sealed chamber was used to maintain control of the solvent annealing climate, as further described in the methods section. From Figure 6b, it is apparent that 10 min solvent anneals in such a system (significantly faster than previously reported[14]) led to lateral ordering and cylinder alignment dramatically improved over templates annealed under ambient conditions for this block copolymer (Figure 1). This is quantified via the fast Fourier transform of the AFM image (the inset to Figure 6b), demonstrating single-crystal hexagonally close packed order. Wider scan ranges provide lateral correlation lengths of order 2.3 μm, at these annealing conditions. In addition, the histogram of feature sizes shown in Figure 6d gives a standard deviation in diameter of 2.5 nm cf. 2.8 nm in the ambient case.

Using these better-ordered polystyrene templates, the patterning process shown in Figure 2 was carried out, resulting in the nanodot array shown in Figure 6c. This image is representative of the entire array, showing clear long-range hexagonally close packed ordering and a significantly reduced dispersion in dot diameter in comparison to the ambient solvent annealing case. The standard deviation is in fact decreased from 3.4 to 1.6 nm, i.e., 13.6 to 6.6%. In addition, the standard deviation in center-to-center spacing is also greatly improved (0.6 nm cf. 3.8 nm), giving a dot spacing distribution of better than 1.5%. Note the slight disparity in the peak positions of the histograms in Figure 6d for the dot array and template, as well as a larger distribution for the template compared to the dot array. This is likely due to problems with exact magnification calibrations in AFM imaging, although sample-tip interactions could also play a role.

Figure 7 compares room temperature, in-plane hysteresis loops obtained for arrays patterned from both the ambient (A) and climate controlled (C) solvent annealed templates. The data are shown on two applied field scales (300 Oe in panel a and 3000 Oe in panel b). The first thing to note about array C is that it possesses significantly higher M_S in comparison to array A. Using the thickness (height) determined from X-ray reflectivity (approximately 27 nm) we obtain $M_s \approx 557$ emu/cm^3, i.e., 66% of the bulk value, increased by 77% cf. array A (a value substantially larger than those found via traditional etching-based pattern transfer methods, as discussed above[24,25]). Using the approach discussed above (which includes shape anisotropy), we estimate that the crossover to superparamagnetism should occur at a thickness of about 6 nm in this case, the lower critical thickness being due to the enhanced M_S, which enters into the shape anisotropy. The ferromagnetic nanodots in array C are thus much deeper into the regime where the ferromagnetism is thermally stable in comparison to array A. This is reflected in Figure 7b as a much more obvious attainment of saturation for array C, and

3479

dx.doi.org/10.1021/am200693x |ACS Appl. Mater. Interfaces 2011, 3, 3472–3481

thus a lower saturation field and higher remanence. The remainder of the differences between the two loops can be simply understood in terms of the distributions in volume and interdot spacing. The large dot volume distribution in array A leads to dot volumes that fall both above and below the superparamagnetic limit. The small volume dots (superparamagnetic) provide small (eventually zero) remanent magnetization and a slow approach to saturation, consistent with Langevin-type behavior. At the same time, the dots in the high volume tail of the distribution are ferromagnetic and provide enhanced coercivity compared to array C. This is due to not only an increase in magnetocrystalline anisotropy energy but also an increase in shape anisotropy due to the flatter "pancake-like" structure. In comparison, the nanodots in array C are well above the calculated superparamagnetic limit and have tighter volume distributions, ensuring a negligible superparamagnetic contribution. The reduced coercivity for array C compared to array A (28 Oe cf. 42 Oe) is likely due to the shape anisotropy in these taller cylinders beginning to favor out-of-plane orientation. In addition to the tighter volume distribution in array C, the decreased dispersion in dot spacings, which are also very different, will lead to a local variation in dipolar coupling between the dots as compared to array A. This effect will also contribute, to some extent, to the differences in the magnetic response of the two arrays. In short, these magnetic results clearly show that this Damascene method of pattern transfer does indeed lead to retention of robust ferromagnetic properties. This is particularly noteworthy given the low magnetocrystalline anisotropy of our test case material (NiFe), which is also known to be susceptible to etch damage.

CONCLUSIONS

From both microscopy and detailed magnetic/electrical characterization as a function of Ar ion beam milling time, the non lift-off Damascene-style patterning process illustrated in Figure 2 leads to high-fidelity transfer of a nanoscale pattern from a PS template to a metallic thin film. This approach is simple, and circumvents some of the most significant challenges with etching and lift-off processes. The process employs solvent annealed cylinder forming PS-PLA BCPs, exploiting the simple aqueous degradation of the minority component, applying six distinct processing steps: spin-casting polymer solution, solvent annealing in THF, aqueous removal of the minority block, reactive ion etch removal of a polymer wetting layer, metal evaporation, and Ar ion beam milling. The process is demonstrated here for 25 nm NiFe nanodots at a density of $(385 \pm 31) \times 10^9$ dots/in^2. It can be expected that this process is extendable to other slow-milling metals and should be amenable to further reductions in feature size. With the recent improvements in cylinder forming BCP templates, particularly with the aid of solvent annealing in climate-controlled conditions, this pattern transfer approach shows remarkable promise for patterning at the extreme nanoscale with high fidelity. Additionally, the process is distinctly advantageous from the point of view of minimization of etch damage to the patterned materials.

ASSOCIATED CONTENT

ⓢ Supporting Information. S1 and S2: A random sampling of $2 \times 2 \ \mu$m^2 AFM height images taken over the course of 1 year of ~50 nm thick films of PS-*b*-PLA (M_n = 63.7 kDa with a polydispersity index of 1.05, with a PLA phase fraction of 0.29

(by volume) yielding a cylindrical morphology) that were solvent annealed with THF in ambient conditions (S1) and in a climate-controlled chamber (S2). S3: Normal incidence Ar ion beam milling dependence on thickness and magnetometry of a continuous 43 nm planar NiFe film (thickness chosen to match the overlayer thickness in the manuscript) on smooth polystyrene (M_n = 42.5 kDa, with spin-cast conditions kept as in the manuscript). This material is available free of charge via the Internet at http://pubs.acs.org/.

AUTHOR INFORMATION

Corresponding Author
*E-mail: leighton@umn.edu (C. L.); hillmyer@umn.edu (M. A. H.).

ACKNOWLEDGMENT

REFERENCES

(1) Hamley, I. W. *Prog. Polym. Sci.* **2009**, *34*, 1161–1210.

(2) Park, S.; Lee, D. H.; Xu, J.; Kim, B; Hong, S. W.; Jeong, U.; Xu, T; Russell, T. P. *Science* **2009**, *323*, 1030–1033.

(3) Olayo-Valles, R.; Lund, M. S.; Leighton, C.; Hillmyer, M. A. *J. Mater. Chem.* **2004**, *14*, 2729–2731. Olayo-Valles, R.; Guo, S.; Lund, M. S.; Leighton, C.; Hillmyer, M. A. *Macromolecules* **2005**, *38*, 10101–10108.

(4) Zhang, X.; Harris, K. D.; Wu, N. L. Y.; Murphy, J. N.; Buriak, J. M. *ACS Nano* **2010**, *4*, 7021–7029.

(5) Morkved, T. L.; Lu, M.; Urbas, A. M.; Ehrichs, E. E.; Jaeger, H. M.; Mansky, P.; Russell, T. P. *Science* **1996**, *273*, 931–933. Thurn-Albrecht, T.; Schotter, J.; Kastle, G. A.; Emley, N.; Shibauchi, T.; Krusin-Elbaum, L.; Guarini, K.; Black, C. T.; Tuominen, M. T.; Russell, T. P. *Science* **2000**, *290*, 2126–2129.

(6) Böker, A.; Knoll, A.; Elbs, H.; Abetz, V.; Muller, A. H. E.; Krausch, G. *Macromolecules* **2002**, *35*, 1319–1325.

(7) Kubo, T; Parker, J. S.; Hillmyer, M. A.; Leighton, C. *Appl. Phys. Lett.* **2007**, *90*, 233113–233115. Kubo, T; Wang, R. F.; Olson, D. A.; Rodwogin, M.; Hillmyer, M. A.; Leighton, C. *Appl. Phys. Lett.* **2008**, *93*, 133112–133114.

(8) Bang, J.; Jeong, U.; Ryu, D. Y.; Russell, T. P.; Hawker, C. J. *Adv. Mater.* **2009**, *21*, 1.

(9) Yang, J. K. W.; Jung, Y. S.; Chang, J. -B.; Mickiewicz, R. A.; Alexander-Katz, A.; Ross, C. A.; Berggren, K. K. *Nat. Nanotechnol.* **2010**, *5*, 256–260.

(10) Ruiz, R.; Kang, H.; Detcheverry, F. A.; Dobisz, E.; Kercher, D. S.; Albrecht, T. R.; de Pablo, J. J.; Nealey, P. F. *Science* **2008**, *321*, 936–939.

(11) Bosworth, J. K.; Paik, M. Y.; Ruiz, R.; Schwartz, E. L.; Huang, J. Q.; Ko, A. W.; Smilgies, D. -M.; Black, C. T.; Ober, C. K. *ACS Nano* **2008**, *2*, 1396–1402.

(12) Liang, G. -D.; Xu, J. -T.; Fan, Z. -Q. *J. Phys. Chem. B* **2007**, *111*, 11921–11928.

(13) Cavicchi, K. A.; Russell, T. P. *Macromolecules* **2007**, *40*, 1181–1186.

(14) Vayer, M.; Hillmyer, M. A.; Dirany, M.; Thevenin, G.; Erre, R.; Sinturel, C. *Thin Solid Films* **2010**, *518*, 3710–3715.

(15) Cavicchi, K. A.; Berthiaume, K. J.; Russell, T. P. *Polymer* **2005**, *46*, 11635–11639.

(16) Kim, S. H.; Misner, M. J.; Xu, T.; Kimura, M.; Russell, T. P. *Adv. Mater.* **2004**, *16*, 226–231.

(17) Phillip, W. A.; Hillmyer, M. A.; Cussler, E. L. *Macromolecules* **2010**, *43*, 7763–7770.

(18) Black, C. T.; Guarini, K. W.; Milkove, K. R.; Baker, S. M.; Russell, T. P.; Tuominen, M. T. *Appl. Phys. Lett.* **2001**, *79*, 409–411.

(19) Guarini, K. W.; Black, C. T.; Zhang, Y.; Kim, H.; Sikorski, E. M.; Babich, I. V. *J. Vac. Sci. Technol. B* **2002**, *20*, 2788–2792.

(20) Shin, K.; Leach, K. A.; Goldbach, J. T.; Kim, D. H.; Jho, J. Y.; Tuominen, M.; Hawker, C. J.; Russell, T. P. *Nano Lett.* **2002**, *2*, 933.

(21) Xiao, S.; Yang, X. M.; Edwards, E. W.; La, Y. −H.; Nealey, P. F. *Nanotechnology* **2005**, *16*, S324–S329.

(22) Vieu, C.; Carcenac, F.; Pepin, A.; Chen, Y.; Mejias, M.; Lebib, A.; Manin-Ferlazzo, L.; Couraud, L.; Launois, H. *Appl. Surf. Sci.* **2000**, *164*, 111–117.

(23) Knapp, J. A.; Borgesen, P.; Zuhr, R. A., Eds.; *Beam-Solid Interactions: Physical Phenomena*; MRS Proceedings; Materials Research Society: Warrendale, PA, 1990; Vol. 157.

(24) Li, X.; Tadisina, Z. R.; Guptaa, S. *J. Vac. Sci. Tech. A* **2009**, *27*, 1062.

(25) Ilievski, F.; Ross, C. A.; Vancso, G. J. *J. Appl. Phys.* **2008**, *103*, 07C520.

(26) McMichael, R. D.; Ross, C. A.; Chuang, V. P. *J. Appl. Phys.* **2008**, *103*, 07C505. Zhu, M.; McMichael, R. D. *J. Appl. Phys.* **2011**, *109*, 043904.

(27) Cheng, J. Y.; Ross, C. A.; Chan, V. Z.-H.; Thomas, E. L.; Lammertink, R. G. H.; Julius Vancso, G. *Adv. Mater.* **2001**, *13*, 1174.

(28) Terris, B. D.; Thomas, T. *J. Phys. D: Appl. Phys.* **2005**, *38*, R199.

(29) Ross, C. A.; Cheng, J. Y. *MRS Bull.* **2008**, *33*, 838.

(30) Rettner, C. T.; Anders, S.; Baglin, J. E. E.; Thomson, T.; Terris, B. D. *Appl. Phys. Lett.* **2002**, *80*, 279.

(31) Krycka, K. L.; Maranville, B. B.; Borchers, J. A.; Castaño, F. J.; Ng, B. G.; Perkinson, J. C.; Ross, C. A. *J. Appl. Phys.* **2009**, *105*, 07C120.

(32) Min, J. -H.; Hwang, S. -H.; Lee, G. -R.; Moon, S. H. *J. Vac. Sci. Technol. B* **2003**, *21*, 2198–2204.

(33) Jung, Y. S.; Ross, C. A. *Small* **2009**, *5*, 1654–1659.

(34) Cui, Z. *Nanofabrication: Principles, Capabilities and Limits*; Springer: New York, 2008; p 229.

(35) Jung, Y. S.; Lee, J. H.; Lee, J. Y.; Ross, C. A. *Nano Lett.* **2010**, *10*, 3722–3726.

(36) Nagato, K; Toyoda, N.; Naito, H.; Tani, H.; Sakane, Y.; Yamada, I.; Nakao, M.; Hamaguchi, T. *J. Appl. Phys.* **2011**, *109*, 07B733.

(37) Nagato, K; Hoshino, H.; Naito, H.; Hirota, T.; Tani, H.; Sakane, Y.; Toyoda, N.; Yamada, I.; Nakao, M.; Hamaguchi, T. *IEEE Trans. Magn.* **2010**, *46*, 2504.

(38) Yamada, I.; Matsuo, J.; Toyoda, N.; Kirkpatrick, A. *Mat. Sci. and Eng. R* **2001**, *34*, 231–295.

(39) ImageJ, a public domain Java image processing program inspired by NIH Image for the Macintosh. Details at http://rsb.info.nih.gov/ij/

(40) Winklhofer, M.; Dumas, R. K.; Liu, K. *J. Appl. Phys.* **2008**, *103*, 07C518.

(41) These samples are deposited on heavily doped Si wafers, thus conductive pathways exist via the substrate at 300 K; however, these pathways are effectively shut off in the 5 K data.

(42) O'Handley, R. C. *Modern Magnetic Materials: Principles and Applications*; Wiley: New York, 2000; p 192.

(43) Néel, L. *Ann. Geophys. (C.N.R.S.)* **1949**, *5*, 99.

(44) Chen, D. -X.; Brug, J. A.; Goldfarb, R. B. *IEEE Trans. Magn.* **1991**, *27*, 3601–3619.

(45) Scholz, W.; Guslienko, K. Yu.; Novosad, V.; Suess, D.; Schrefl, T.; Chantrell, R. W.; Fidler, J. *J. Magn. Magn. Mater.* **2003**, *266*, 155–163.